The International Journal of Engineering and Science (IJES)
|| Volume || 10 || Issue || 4 || Series I || Pages || PP 24-31|| 2021 ||
ISSN (e): 2319-1813 ISSN (p): 20-24-1805

Comparison of Landsat 8 (OLI) and Landsat 7 (ETM+) satellite Remote Sensing data in automatic lineaments extraction: A case study of Nkolezom, southern part of Cameroon

Tchato Sandra Céleste[1], Fossi Donald Hermann[2], Kamto Paul Gautier[1], Deassou Sezine Eric[3], Lemotio Willy[1], Bidichael Wahilé Waffouo Elvis[3]

[1]*National Institute of Cartography, P.O. Box 157 Yaounde Cameroon*
[2]*Institute of Geological and Mining Research, P.O. Box 4110 Yaounde Cameroon*
[3]*Faculty of Science, University of Yaounde I, P.O. Box 812 Yaounde, Cameroon*
Corresponding Author: Tchato Sandra Céleste

--ABSTRACT--

The lineament mapping and analysis through Remote sensing and Geographical Information System (GIS) technology occupies an important place in several fields of structural geological investigation. In this study, remote sensing applications through the processing of Landsat-7 ETM+ and Landsat-8 OLI/TIRS were used to assess their ability in automatic lineament identification and extraction. In addition to satellite data, the pre-existing geological map was used. After finding the optimal parameters of the LINE module for automatic lineament extraction in the study area, the comparison and validation of obtained results were undertaken. It appears that the lineaments extracted from Landsat-8 are better correlated with the faults in the study area both in terms of spatial distribution and orientation. The latter is more efficient in lineament mapping.

KEYWORDS*: Landsat-8 OLI/TIRS, Landsat-7 ETM+, Remote sensing, Geographical information system, Automatic lineament extraction.*

Date of Submission: 27-03-2021 Date of Acceptance: 10-04-2021

I. INTRODUCTION

The growing interest in Geographic Information System (GIS) and remote sensing technology has increased their application in various fields of study such as geology, hydrogeology, mining exploration etc. Since more than two decades, satellite imagery has been used for the identification and mapping of geologic structures which appear in geomorphology [1,2]. However, these geologic structures can be identified by lineament mapping, which is an important part of structural geology and they reveal the architecture of the underlying rock basement [3]. Lineament mapping plays a major role in geological studies, especially in mining and petroleum exploration [4]. Moreover, the localization of lineaments often close to several mineralogical deposits [5–7] qualifies them as an indirect indicator of mining potential [8]. Lineaments can be an expression on the ground surface of structural elements such as joints, faults, bedding plains, shear zones, fractures, fold hinges and foliation [9–11]. The latter may correspond to geologic structures (faults, joints, fracture traces, line weakness), geomorphic features (cliffs, structural ridges, terraces, linear valleys), tonal contrast (vegetation, soil moisture, rock composite) and anthropogenic features (roads, electric grids, railways etc.). Because of being hard and time-consuming, conventional ground-based mapping techniques are not efficient for structural geological studies of humid tropical regions due to the important vegetation cover and the thick terrigenous materials recovery [12], hence the need to use satellite images. Therefore, the speed and accuracy of lineament extraction have enhanced efficiently due to remote sensing and GIS techniques providing a synoptic view of any particular area [13]. Multispectral and high-resolution images prove to be a powerful and accurate tool in delineating structural discontinuities. Indeed, a number of authors used multispectral satellite images including Landsat 7 (ETM+) and Landsat 8 (OLI/TIRS) to identify and extract the structural lineaments [8,14–16]. Lineament identification and extraction in remote sensing can be carried out through two approaches including manual extraction, which mainly depends on visual interpretation and general knowledge of interpreter [3]; and automatic lineament extraction using computer software and algorithms [17,18]. Several studies have been carried out to extract lineaments automatically using computer algorithms. Many researchers used Hough Transformation [19–21], LINE module of PCI Geomatica [22,8,15], Multi-Hillshade Hiearchic Clustering (MHHC) [23]. Though there are various methods of automatic lineament extraction, this work will only consider the LINE module of PCI Geomatica. The aim of the present study is to compare the ability of Landsat

8 (OLI/TIRS) and Landsat 7 (ETM+) in automatic lineament extraction in the study area, using remote sensing techniques. This study is only interested in structural lineaments.

II. GEOLOGICAL SETTING OF THE STUDY AREA

The Study area (Figure 1) belongs to the Ntem Complex which represents the north-western extension of the Congo Craton in southern part of Cameroon [24-25] and lies in latitude 2º34'4 N to 2º51'N and longitude 11º27'E to 11º45'E. This complex is made up of two main lithological groups, namely the Nyong and Ntem Groups. The Nyong Unit consists mainly of gneisses, amphibolites, metagranodiorites, metadolerites, micaschists, quartzites, serpentinites and eclogites; while the Ntem Unit Comprised High-K granites, syenites, charnockites, gneisses, and tonalite-trondhjemite-granodiorite suite. BIFs generally occur in greenstone belts throughout the Ntem Complex, and host gold mineralization and iron ore deposits [26–30]. The basement rocks of study area consist of basalt, rhyolite, granites, gneiss and migmatites.

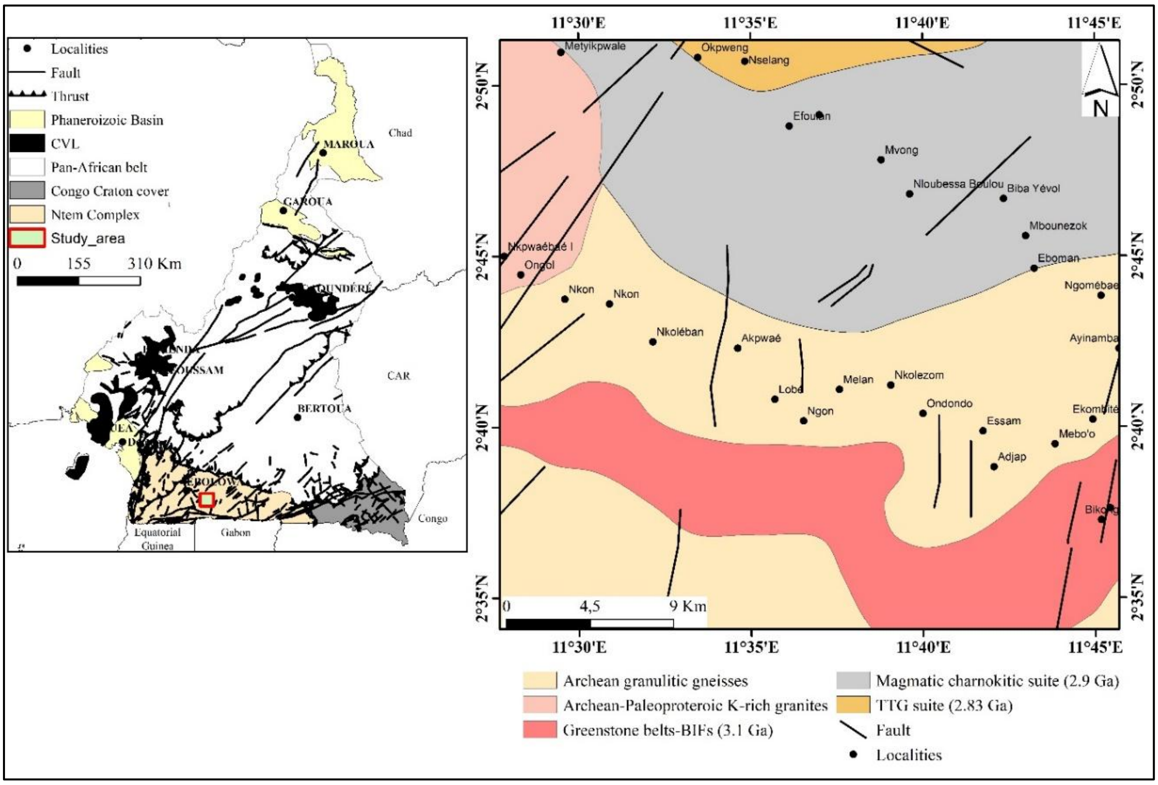

Figure. 1. Geological map of the study area

III. MATERIALS AND METHODS

III.1 Data sources

Two types of data were used in this study, these included Landsat 8 OLI/TIRS image (dated 26-01-2020, Path 185/ Row 58) and Landsat 7 ETM+ image (dated 07-04-2020, Path 185/ Row 58), corresponding to Zone 32 of the map projection, Universal Transverse Mercator (UTM) which uses the geodetic reference system WGS 84. Lineaments was extracted automatically from Pan-Sharpened Landsat 8 and Landsat 7 images using image processing and visual interpretation techniques. The Landsat-8 OLI/TIRS consist a free of cloud terrain-corrected scene, which comprises 11 bands (coastal aerosol, blue, green, red, near infrared, two shortwave infrareds, panchromatic, cirrus, and two thermal infrareds; table 1). Regarding to Landsat 7 ETM+, it consists a 4% of cloud terrain-corrected scene with nine bands (blue, green, red, near infrared, two medium infrareds, and two thermal infrareds and panchromatic; table 1). In order to derive details concerning lineament distribution, geospatial analysis was performed for the consequent structural lines. With the support of the Rockworks 17 software, the lineament orientation was formed as a Rose diagram.

III.2 Processing

[31] described digital image processing as an image manipulation method with the help of computer software besides greater image resolution. Throughout this ongoing project, the image processing was done as follows.

III.2.1 Image sharpening

In many studies, pan-sharpening has proven to be a useful tool for identifying, extracting, and separating lineaments [22,10,32,33]. The latter has many algorithms, such as IHS (Intensity Hue Saturation), Brovey, Gram-Schmidt [34,35]. For this study, the Gram-Schmidt pan-sharpening algorithm was used on Landsat-8 and Landsat-7 images in the ENVI 5.3 program.

Landsat 8 OLI/TIRS			*Landsat 7 ETM+*		
Spectral range	***Wavelength range (µm)***	***Resolution (m)***	***Spectral range***	***Wavelength range (µm)***	***Resolution (m)***
B1-Coastal /aerosol	0.433-0.453	30			
B2- Blue	0.450-0.515	30	B1-Blue	0.45-0.52	30
B3- Green	0.525-0.600	30	B2- Green	0.52-0.60	30
B4- Red	0.630-0.680	30	B3- Red	0.63-0.69	30
B5- NIR	0.845-0.885	30	B4-NIR	0.77-0.90	30
B6- SWIR 1	1.56-1.66	30	B5-SWIR1	1.55-1.75	30
B7-SWIR 2	2.10-2.30	30	B7- SWIR2	2.09-2.35	30
B8- Panchromatic	0.50-0.68	15	B8- Panchromatic	0.52-0.90	15
B9- Cirrus	1.36-1.39	30			
B10- TIRS 1	10.3-11.3	100	B6/1- TIR B6/2- TIR	10.40-12.50	60
B11- TIRS 2	11.5-12.5	100			120

Table 1. The spectral bands and resolutions of Landsat-8 and Landsat 7 datasets used in this study.

III.2.2 Principal Component Analysis

The Principal Component Analysis (PCA) which is a statistical method widely used in geological studies to eliminate the redundancy of data, isolates noise, and then enhances the targeted information in the image [36], has proven to be effective in its use for lineament identification. Indeed, [37] compared five different enhancement techniques (average value of all bands, PCA, Band Ratios (BR), histogram equalization and high pass filter) performed by [38] and PCA was found to be more efficient in the identification of lineaments. Several authors used it for mapping lineaments [13,28,39]. Then, PCA transformation was performed using six channels of Landsat-8 (band 2, 3, 4, 5, 6, and 7) and Landsat-7 (1, 2, 3, 4, 5, and 7). All these channels of each dataset have the same resolution, 30 m. This operation was done through ENVI 5.3 software and the first component of PCA for Landsat-8, and the second component of PCA for Landsat-7 were retained at the end of this operation, and exported to TIFF.

III.3. Automated lineament extraction

Lineaments were extracted from multispectral images used automatic lineament extraction. These was performed used the LINE module in PCI Geomatica software. The two TIFFs (Figure 2 a, b) from ENVI 5.3 were planned and then imported into the PCI Geomatica LINE module. Three measures of parameters matching the software algorithm are edge detection (RADI: filter radius), threshold detection (GTHR: Edge Gradient Threshold) and curve detection (LTHR: Curve Length Threshold; FTHR:Line Fitting Threshold; ATHR:Angular Difference Threshold; DTHR :Linking Distance Threshold) to extract lineaments. The lines of a raster image are specified in the LINE module and translated into vector formats, based on six parameters [40] provided in table 2.

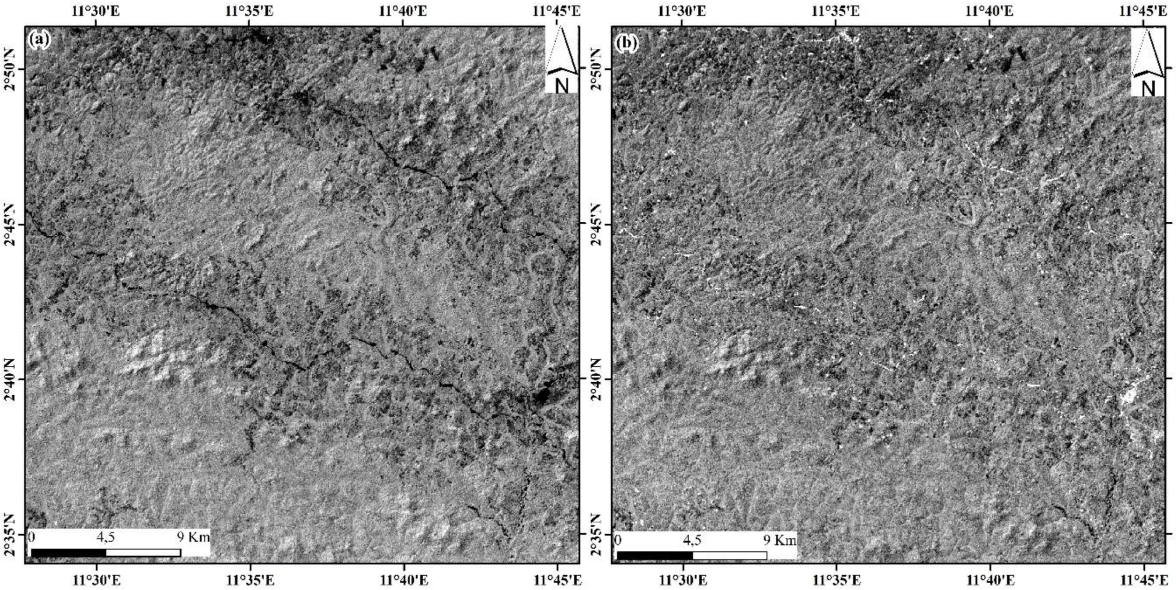

Figure 2. Principal components (**a**) (PC1) and (**b**) (PC2) of OLI and ETM+ sensors respectively.

Table 2. The values used for the parameters of the LINE module.

Threshold parameters and units	*Default values*	*Selected values*
RADI (In pixels)	10	8
GTHR (In range, 0–255)	100	50
LTHR (In pixels)	30	25
FTHR (In pixels)	3	3
ATHR (In degrees)	30	10
DTHR (In pixels)	20	20

IV. RESULTS AND DISCUSSIONS

Image pre-processing techniques such as pan sharpening are applied to the data in order to prepare them for the processing step. The application of processing methods in different image (Figure 2a, b) lead to a lineament map of the study area (Figure 3a, b). The statistic information presented in fig. 6 shows that 873 and 884 lineaments were identified and extracted from the Landsat-8 and Landsat-7 images respectively.

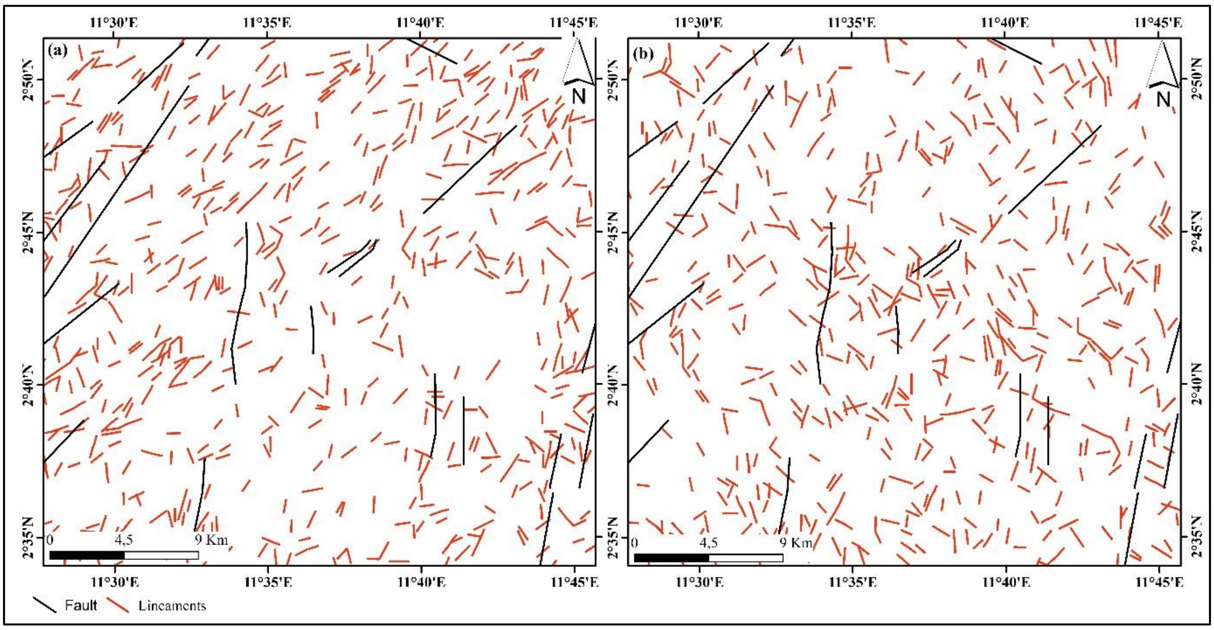

Figure 3. Lineament map of the study area obtained from (**a**) OLI and (**b**) ETM+ sensors respectively

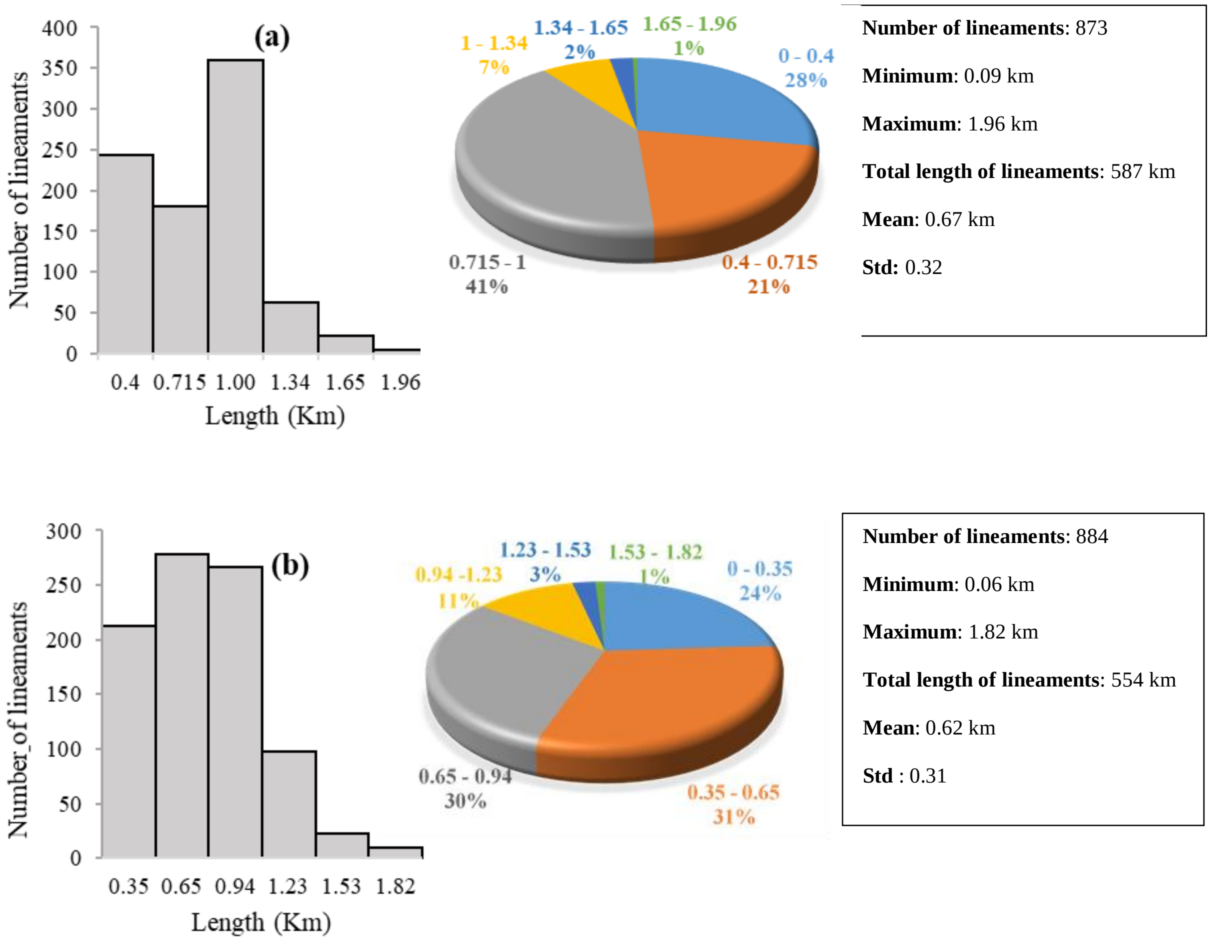

Figure 4. Distribution histograms showing the number of lineaments according to the length for the (**a**) OLI and (**b**) ETM+ images.

According to the statistic, the Landsat- 8 length values range from 90 m to 1.96 km (Figure 4a). The most abundant lineaments lengths are between 0.71 and 1 Km (360) that occupy 41% of the total number of extracted lineaments. The Landsat- 7 length values range between 60 m to 1.82 km (Figure 4b). The most dominating lengths of extracted lineaments are extended between 0.35 and 0.65 km (278) corresponding to 31% of the total number of extracted lineaments. By comparing the obtained statistics, one can notice that the total number of lineaments extracted from each of the used data are nearly similar. However, in general the lineaments extracted from the OLI image turn out to be longer than those extracted from the ETM+ image.

IV.1 Accuracy assessment

IV.1.1 Density

A density map is a classification map that provides information about lineaments concentration per unit area [41]. The lineament density maps in this study are derived for each of OLI and ETM+ lineament maps, in order to analyze the lineaments dispersion pattern. This task was performed using line density tool of the spatial analyst in ArcGIS 10.5 software. The highest density values on the maps are represented by a red color, while the lowest values are in green. In this work, the density was also used to find the correlation between the lineaments concentration and the existing faults distribution. The lineaments extracted from Landsat-7 (Figure 5b) present the high density values concentrated mainly in the South-east of the image. Most of the faults are located near low and average density areas. Regarding to the Landsat-8 image, the extracted lineaments (Figure 5a) show the high density values concentrated in the Northeastern, Northern and Southwestern parts of the image. Most of these high density values are located near the faults of the study area. The results obtained from the OLI sensor showed a better correlation with the distribution of the faults. Areas with high density values could indicate areas with mining potential.

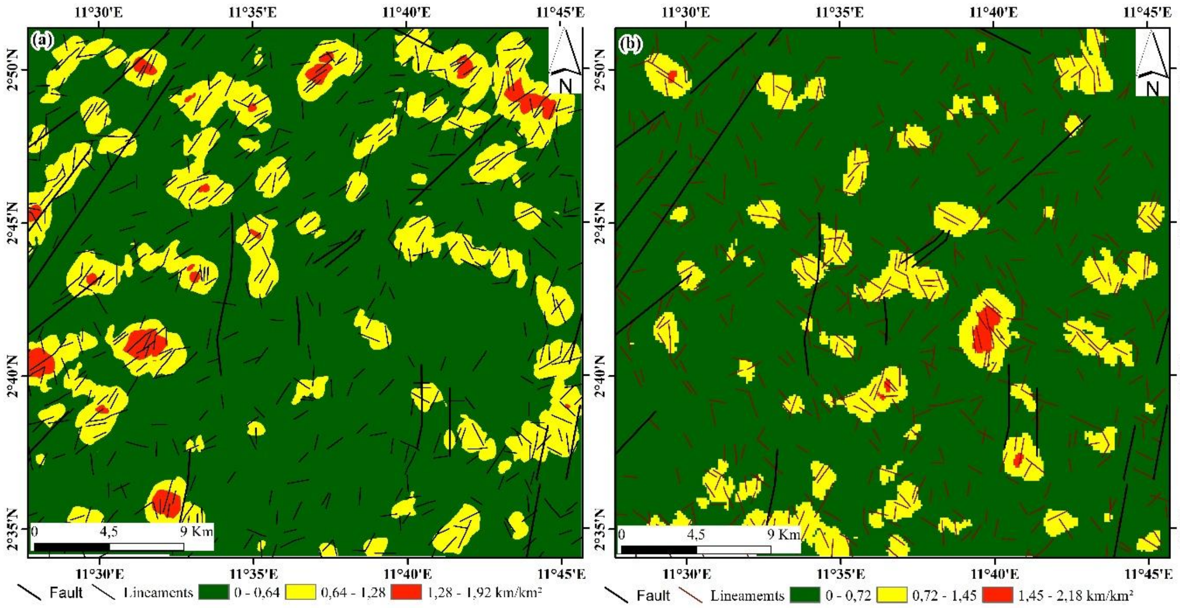

Figure 5. Correlation between the density of lineaments and the location of the faults for the (**a**) OLI and (**b**) ETM+ images

IV.1.2 Orientation

The orientation allows identifying the most frequent directions of lineaments. Therefore, they can be compared with directions relating to existing faults in the study area [5,42]. Lineament orientation is analyzed by creating rose diagrams for each of the lineament maps, which allow highlighting the number of most frequent lineaments in a particular direction. The directional rosettes are then produced with an angular spacing of 15° and without using the frequency (Figure 6).

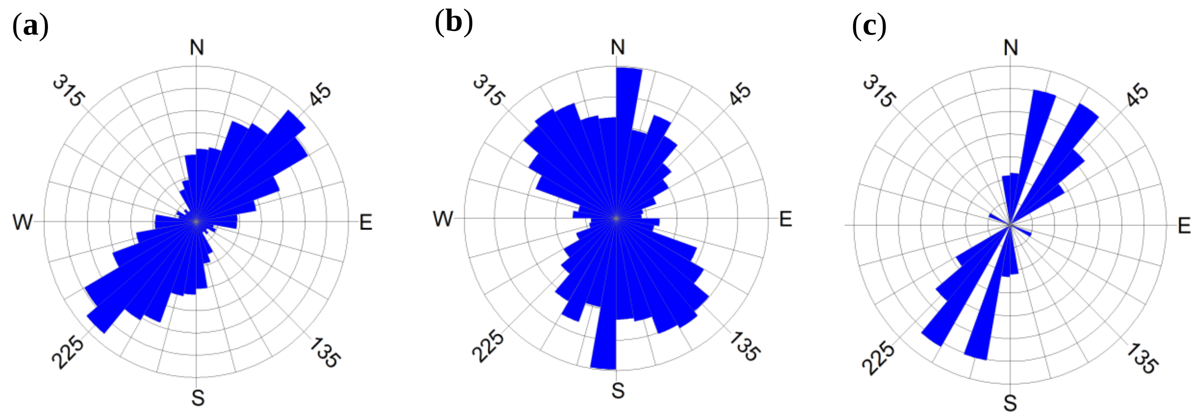

Figure 6. Orientations of lineaments obtained from the (**a**) OLI and (**b**) ETM+ images comparing to those of (**c**) the faults of the study area.

This procedure has been done using Rockworks 17 software. The rose diagram shows the orientations of lineament with the dominance of NE-SW direction for the OLI image (Figure 6a). The latter shows a good correlation with that of the faults of the study area. Regarding the ETM+ image, the N-S and NW-SE are shown as majority directions (Figure 6b).

V. CONCLUSION

The main objective of this study was to evaluate the ability of Landsat-8 and Landsat-7 in automatic lineament extraction. After image processing including PCA, the comparison of gained results indicates that the best bands for this extraction are PC1 and PC2 for Landsat-8 and Landsat-7 respectively. By comparing the statistics of the extracted lineaments for each of the used data, it emerges that the Landsat-8 and Landsat-7 images nearly resulted in the same number of extracted lineaments. Furthermore, the comparison of the obtained results while including pre-existing geological map, density, orientation, compared to the pre-existing faults showed that, Landsat-8 gives better results than Landsat-7. The Landsat-8 lineaments converge better with the localization and the orientation of the existing faults in the study area than Landsat-7 ones. This result can be explained by the fact that Landsat-8 has narrower spectral bands compared to Landsat-7.

REFERENCE

[1]. Parsons A J and Yearley R J 1986 An analysis of geologic lineaments seen on LANDSAT MSS imagery *Int. J. Remote Sens.* **7** 1773–82

[2]. Ozer A, Marion J-M, Roland C and Tréfois P 1988 Signification de linéaments sur une image SPOT dans la région liégeoise *Bull. Société Belge Géologie* **97** 153–72

[3]. Ramli M F, Yusof N, Yusoff M K, Juahir H and Shafri H Z M 2010 Lineament mapping and its application in landslide hazard assessment: a review *Bull. Eng. Geol. Environ.* **69** 215–33

[4]. Marghany M and Hashim M 2010 Lineament mapping using multispectral remote sensing satellite data *Int. J. Phys. Sci.* **5** 1501–7

[5]. Meshkani S A, Mehrabi B, Yaghubpur A and Sadeghi M 2013 Recognition of the regional lineaments of Iran: Using geospatial data and their implications for exploration of metallic ore deposits *Ore Geol. Rev.* **55** 48–63

[6]. Pour A B and Hashim M 2014 ASTER, ALI and Hyperion sensors data for lithological mapping and ore minerals exploration *SpringerPlus* **3** 130

[7]. Pour A B, Hashim M, Makoundi C and Zaw K 2016 Structural Mapping of the Bentong-Raub Suture Zone Using PALSAR Remote Sensing Data, Peninsular Malaysia: Implications for Sediment-hosted/Orogenic Gold Mineral Systems Exploration *Resour. Geol.* **66** 368–85

[8]. Adiri Z, El Harti A, Jellouli A, Lhissou R, Maacha L, Azmi M, Zouhair M and Bachaoui E M 2017 Comparison of Landsat-8, ASTER and Sentinel 1 satellite remote sensing data in automatic lineaments extraction: A case study of Sidi Flah-Bouskour inlier, Moroccan Anti Atlas *Adv. Space Res.* **60** 2355–67

[9]. O'leary D W, Friedman J D and Pohn H A 1976 Lineament, linear, lineation: Some proposed new standards for old terms *GSA Bull.* **87** 1463–9

[10]. Hung L Q, Batelaan O and Smedt F D 2005 Lineament extraction and analysis, comparison of LANDSAT ETM and ASTER imagery. Case study: Suoimuoi tropical karst catchment, Vietnam *Remote Sensing for Environmental Monitoring, GIS Applications, and Geology V* Remote Sensing for Environmental Monitoring, GIS Applications, and Geology V vol 5983 (International Society for Optics and Photonics) p 59830T

[11]. Soesilo I and Hoppin R A 1986 Evaluation of digitally processed Landsat imagery and SIR-A imagery for geological analysis of West Java region, Indonesia Remote sensing for ressources development and environmental management. International symposium. 7 pp 173–82

[12]. Faillat J-P 1986 Hétérogénéité et effet d'échelle dans les aquifères fissurés. Approche par pompage d'essai sur station expérimentale (Afrique de l'Ouest) *Hydrogéologie* **1** 65–76

[13]. Takodjou Wambo J D, Ganno S, Ngambu A A, Negue E N, Mvondo Ondoa J and Nzenti J P 2016 Use of landsat 7 ETM+ Data for the geological structure interpretation: case study of the Ngoura-Colomines Area, Eastern Cameroon *J. Geosci.* **4** 61–72

[14]. Salui C L 2018 Methodological Validation for Automated Lineament Extraction by LINE Method in PCI Geomatica and MATLAB based Hough Transformation *J. Geol. Soc. India* **92** 321–8

[15]. Javhar A, Chen X, Bao A, Jamshed A, Yunus M, Jovid A and Latipa T 2019 Comparison of Multi-Resolution Optical Landsat-8, Sentinel-2 and Radar Sentinel-1 Data for Automatic Lineament Extraction: A Case Study of Alichur Area, SE Pamir *Remote Sens.* **11** 778

[16]. Singh K, Arya A K and Agarwal K K 2020 Landslide Occurrences Along Lineaments on NH-154A, Chamba, Himachal Pradesh; Extracted from Satellite Data Landsat 8, India *J. Indian Soc. Remote Sens.* **48** 791–803

[17]. Morris K 1991 Using Knowledge-Base Rules to Map the Three-Dimensional Nature of Geological *Photogramm. Eng. Remote Sens.* **57** 1209–16

[18]. Prasad A D, Jain K and Gairola A 2013 Mapping of lineaments and knowledge base preparation using geomatics techniques for part of the Godavari and Tapi basins, India: A case study *Int. J. Comput. Appl.* **70**

[19]. Wang J and Howarth P J 1990 Use of the hough transform in automated lineament *IEEE Trans. Geosci. Remote Sens.* **28** 561–7

[20]. Karnieli A, Meisels A, Fisher L and Arkin Y 1996 Geological Linear Features from Digital Remote Sensing Data Using a Hough Transform *Photogramm. Eng. Remote Sens.* **62** 525–31

[21]. Argialas D P and Mavrantza O D 2004 Comparison of edge detection and Hough transform techniques for the extraction of geologic features *Int. Arch. Photogramm. Remote Sens. Spat. Inf. Sci.* **34**

[22]. Kocal A, Duzgun H S and Karpuz C 2004 Discontinuity mapping with automatic lineament extraction from high resolution satellite imagery *ISPRS XX Istanb.* 12–23

[23]. Šilhavỳ J, Minár J, Mentlík P and Sládek J 2016 A new artefacts resistant method for automatic lineament extraction using Multi-Hillshade Hierarchic Clustering (MHHC) *Comput. Geosci.* **92** 9–20

[24]. Bessoles B and Trompette M 1980 Géologie de l'Afrique: la chaîne Panafricaine,«Zone mobile d'Afrique centrale (partie sud) et Zone mobile soudanaise», Mem *BRGM* **92** 396

[25]. Maurizot P, Abessolo A, Feybesse J L and Lecomte P J 1986 Etude de prospection minière du Sud-Ouest Cameroun: Synthèse des travaux de 1978 à 1985. Rapp. BRGM. 85, CMR 066

[26]. Soh Tamehe L, Ganno S, Kouankap Nono D G, Ngnotue T, Kankeu B and Nzenti J P 2014 Stream sediment geochemical survey of Gouap-Nkollo prospect, southern Cameroon: implications for gold and LREE exploration *Am. J. Min. Metall.* **2** 8–16

[27]. Soh Tamehe L, Nzepang Tankwa M, Chongtao W, Ganno S, Ngnotue T, Nono G D K, Simon S J, Zhang J and Nzenti J P 2018 Geology and geochemical constrains on the origin and depositional setting of the Kpwa–Atog Boga banded iron formations (BIFs), northwestern Congo craton, southern Cameroon *Ore Geol. Rev.* **95** 620–38

[28]. Binam Mandeng E P, Bondjè Bidjeck L M, Takodjou Wambo J D, Taku A, Bineli Betsi T, Solange Ipan A, Tchami Nfada L and Bitom Dieudonné L 2018 Lithologic and structural mapping of the Abiete–Toko gold district in southern Cameroon, using Landsat 7 ETM+/SRTM *Comptes Rendus Geosci.* **350** 130–40

[29]. Nguimatsia Dongmo F W, Chapman R J, Bolarinwa A T, Yongue R F, Banks D A and Olajide-Kayode J O 2019 Microchemical characterization of placer gold grains from the Meyos-Essabikoula area, Ntem complex, southern Cameroon *J. Afr. Earth Sci.* **151** 189–201

[30]. Fuanya C, Bolarinwa A T, Kankeu B, Yongue R F, Tangko E T and Nkepguep F Y 2019 Geochemical characteristics and petrogenesis of basic rocks in the Ako'ozam–Njabilobe area, Southwestern Cameroon: implications for Au genesis *SN Appl. Sci.* **1** 1–12

[31]. Drury S A 1987 Image interpretation in geology *Geocarto Int.* **2** 48–48

[32]. Mogaji K A, Aboyeji O S and Omosuyi G O 2011 Mapping of lineaments for groundwater targeting in the basement complex region of Ondo State, Nigeria, using remote sensing and geographic information system (GIS) techniques *Int. J. Water Resour. Environ. Eng.* **3** 150–60

[33]. Radaideh O M A, Grasemann B, Melichar R and Mosar J 2016 Detection and analysis of morphotectonic features utilizing satellite remote sensing and GIS: An example in SW Jordan *Geomorphology* **275** 58–79

[34]. Aiazzi B, Alparone L, Baronti S and Selva M 2007 MS þ Pan image fusion by an enhanced Gram–Schmidt spectral sharpening *26th Earsel Symp. New Dev. Challenges Remote Sens.*, pp 1–2

[35]. Maurer T 2013 HOW TO PAN-SHARPEN IMAGES USING THE GRAM-SCHMIDT PAN-SHARPEN METHOD – A RECIPE *ISPRS - Int. Arch. Photogramm. Remote Sens. Spat. Inf. Sci.* **XL-1/W1** 239–44

[36]. Amer R, Kusky T and El Mezayen A 2012 Remote sensing detection of gold related alteration zones in Um Rus area, Central Eastern Desert of Egypt *Adv. Space Res.* **49** 121–34

[37]. Li N 2010 *Textural and rule-based lithological classification of remote sensing data, and geological mapping in Southwestern Prieska sub-basin, Transvaal Supergroup, South Africa* PhD Thesis (lmu)

[38]. Walsh S J and Mynar F 1986 Landsat digital enhancements for lineament detection *Environ. Geol. Water Sci.* **8** 123–8

[39]. Oyawale A A, Adeoti F O, Ajayi T R and Omitogun A A 2020 Applications of remote sensing and geographic information system (GIS) in regional lineament mapping and structural analysis in Ikare Area, Southwestern Nigeria *J. Geol. Min. Res.* **12** 13–24

[40]. Suzen M L and Toprak V 1998 Filtering of satellite images in geological lineament analyses: An application to a fault zone in Central Turkey *Int. J. Remote Sens.* **19** 1101–14

[41]. Mostafa M E and Qari M Y H 1995 An exact technique of counting lineaments *Eng. Geol.* **39** 5–15

[42]. Hashim M, Ahmad S, Johari M A M and Pour A B 2013 Automatic lineament extraction in a heavily vegetated region using Landsat Enhanced Thematic Mapper (ETM+) imagery *Adv. Space Res.* **51** 874–90

Tchato Sandra Céleste, et. al. "Comparison of Landsat 8 (OLI) and Landsat 7 (ETM+) satellite Remote Sensing data in automatic lineaments extraction: A case study of Nkolezom, southern part of Cameroon." *The International Journal of Engineering and Science (IJES)*, 10(04), (2021): pp. 24-31.